

Fast Computation of Hemodynamic Sensitivity to Lumen Segmentation Uncertainty

Sethuraman Sankaran*, Leo Grady, and Charles A. Taylor

Abstract—Patient-specific blood flow modeling combining imaging data and computational fluid dynamics can aid in the assessment of coronary artery disease. Accurate coronary segmentation and realistic physiologic modeling of boundary conditions are important steps to ensure a high diagnostic performance. Segmentation of the coronary arteries can be constructed by a combination of automated algorithms with human review and editing. However, blood pressure and flow are not impacted equally by different local sections of the coronary artery tree. Focusing human review and editing towards regions that will most affect the subsequent simulations can significantly accelerate the review process. We define geometric sensitivity as the standard deviation in hemodynamics-derived metrics due to uncertainty in lumen segmentation. We develop a machine learning framework for estimating the geometric sensitivity in real time. Features used include geometric and clinical variables, and reduced-order models. We develop an anisotropic kernel regression method for assessment of lumen narrowing score, which is used as a feature in the machine learning algorithm. A multi-resolution sensitivity algorithm is introduced to hierarchically refine regions of high sensitivity so that we can quantify sensitivities to a desired spatial resolution. We show that the mean absolute error of the machine learning algorithm compared to 3D simulations is less than 0.01. We further demonstrate that sensitivity is not predicted simply by anatomic reduction but also encodes information about hemodynamics which in turn depends on downstream boundary conditions. This sensitivity approach can be extended to other systems such as cerebral flow, electro-mechanical simulations, etc.

Index Terms—Blood flow simulations, machine learning, multi-resolution analysis, segmentation accuracy, sensitivity analysis.

I. INTRODUCTION

ISCHEMIA caused by obstructive coronary artery disease (CAD) is a serious ailment that can lead to severe adverse events including myocardial infarction and death if left untreated. Percutaneous coronary intervention (PCI) using stents and bypass grafting are popular treatment options for patients diagnosed with CAD. In the former, a catheter is inserted in the lumen of a lesion which is suspected to cause ischemia, and a balloon is inflated to restore the lumen to its healthy diameter.

A stent is typically placed during angioplasty to ensure the artery remains permanently open. Another option is to perform a coronary artery bypass graft (CABG) surgery, where the diseased or occluded regions are bypassed using either native artery (such as Internal Mammary artery) or vein graft (e.g., Saphenous vein).

The FAME study [1] demonstrated that the use of fractional flow reserve (FFR) to decide which lesions need to be stented has a superior performance compared to stenting all vessels with anatomical narrowing. Fractional flow reserve is defined as the ratio of blood flow rate under maximum hyperemia (reduced microvascular resistance achieved by injecting adenosine) to the blood flow under the hypothetical condition that the coronary artery was healthy [2]. Assuming that flow-rate is linearly related to pressure drop, the FFR can be approximated by the ratio of blood pressure distal to a lesion to the blood pressure proximal to the lesion. Current noninvasive tests for CAD either provide data on anatomic narrowing (e.g., via coronary computed tomography angiography (cCTA)) or data on myocardial perfusion deficits (e.g., single photon emission computed tomography (SPECT)), but cannot identify whether specific coronary lesions are functionally significant. It has been demonstrated recently that the FFR can be computed non-invasively from CT-scans (called FFR_{CT}) using blood flow simulations performed on reconstructed coronary lumen segmentation [2]. Three clinical trials have demonstrated the high accuracy that can be achieved using blood flow simulations compared to the invasive gold standard, measured FFR [3]–[5].

Uncertainty in blood flow simulations can be caused by different sources such as artifacts/noise in cCTA, uncertainty in the enforced boundary conditions or uncertainty in the system properties such as blood viscosity. Previous studies suggest that the impact of inaccuracies in lumen segmentation can significantly impact blood flow simulations [6], [7]. Accurate lumen segmentation continues to remain a challenge due to complexity and artifacts related to obtaining cCTA [8], [9]. Evidence from Voros *et al.* [10] suggests that a calcium blooming artifact can increase the minimum lumen diameter by $\sim 40\%$ and can increase overall luminal diameter by $\sim 20\%$, which in turn affects clinical diagnosis. Hence, there is a need to understand how uncertainty in the reconstructed lumen segmentation affects FFR_{CT}, and subsequently identify which regions have the maximum impact on predicted values.

Accounting for uncertainty in partial differential equations has been the subject of many studies [11]–[13]. The link between domain geometry and solution to the Navier-Stokes equations cannot be quantified analytically since the geometry influences the solution indirectly by changing the domain of the

Manuscript received March 25, 2015; revised May 18, 2015; accepted June 07, 2015. Date of publication June 16, 2015; date of current version November 25, 2015. Asterisk indicates corresponding author.

*S. Sankaran is with the HeartFlow Inc., Redwood City, CA 94304 USA (e-mail: ssankaran@heartflow.com).

L. Grady and C. A. Taylor are with the HeartFlow Inc., Redwood City, CA 94304 USA.

Color versions of one or more of the figures in this paper are available online at <http://ieeexplore.ieee.org>.

Digital Object Identifier 10.1109/TMI.2015.2445777

computational mesh over which momentum and mass conservation laws are imposed. Hence, this link needs to be studied computationally which has been the subject of study of some previous works [14], [7], [15]. Analysis of variability in minimum lumen diameter in an idealized model revealed that uncertainty quantification may be important in bypass graft design [16]. Cerebral *et al.* [15] found that geometry has the most impact on flow structures in cerebral aneurysms; however, the geometric sensitivity analysis was restricted to how three modelers constructed the anatomical models (lumen segmentation) and did not quantify sensitivity based on a continuum representation of a family of reconstructed geometries. Further, the extensive branching structure and flow competition between different coronary arteries that is present in the coronary circulation was not a feature of the aneurysm models considered. Yet, this was an important first study to quantify the impact of different variables on the flow fields.

Considerable effort can be saved by focusing lumen segmentation time on regions of the coronary arteries that maximally impact FFR_{CT} results. In blood flow simulations in coronary arteries, only a fraction of the coronary tree has significant impact on the prediction of simulation outcome and diagnosis. Statistical sampling methods such as Monte-Carlo have slow convergence rates that scale with the problem size. While stochastic collocation methods have demonstrated much better convergence rates [7], computation of geometric sensitivity information with patient-specific models may still take multiple days.

We accelerate computation of sensitivities using a machine learning approach. The stochastic collocation algorithm [7], [17], [18] is implicitly learned by the machine learning algorithm. Towards this, we pick a set of features comprising geometry, clinical variables, and analytical models, such as analytical solutions for pipe flow parameterized by vessel radii and length, flow rate, and blood viscosity. Initially, we define all centerline points between two bifurcations, a bifurcation and an outlet, or a bifurcation and an ostium, as a section. Uncertainty of the entire section is controlled by a single random variable (the entire section dilates or erodes in unison as we sample the stochastic space). To remove dependence of the sensitivity field on bifurcation location and to obtain better spatial resolution, we developed an adaptive multi-resolution algorithm that refines stochastic space in regions of high sensitivity. This refinement is performed by identifying sections whose sensitivity value exceeds a threshold, and subsequently splitting the section into two subsections where each subsection is controlled by an independent random variable.

The novelties in this work are

- Development and application of a multi-resolution sensitivity algorithm to resolve regions of high sensitivity without incurring a significant overall computational cost. This is particularly useful in the right coronary artery which tends to have fewer bifurcations, and hence long section lengths.
- Computational framework that can use a different probability model for different portions of the lumen segmentation
- Demonstration that sensitivity information encodes richer information than just anatomic narrowing. Towards this,

we show the improvement in performance obtained from using just geometry based features to using clinical and reduced-order model features.

- Quantifying the link between allowable geometric sensitivity and the range of allowable coefficient of variation in lumen area.

The results show that real-time estimation of sensitivity can be achieved with good accuracy compared to the stochastic collocation method. This also helps us understand the allowable error in lumen segmentation for a given bound on the error in FFR_{CT} . The method in this paper is also applicable to measure the impact of segmentation accuracy in other applications such as the MICCAI coarctation CFD challenge [8], electro-mechanical simulations [19], and others.

II. METHODS

In this section, we describe the setup of the equations governing blood pressure and velocity, as well as those governing sensitivities of blood pressure and velocity to geometry. Subsequently, we provide details on calculating geometric sensitivities based on stochastic pressures calculated by solving the stochastic Navier-Stokes equations. Then, we describe the setup of a machine learning framework based on evaluation of three class of features – geometry-based, clinical and reduced order model. Then, we describe an algorithm for multi-resolution sensitivity analysis. Finally, we describe a method to compute bounds in lumen segmentation for a given allowable error in FFR_{CT} .

A. Governing Equations for Blood Flow Simulations

Blood flow in the cardiovascular system can be modeled using the Navier-Stokes equations which are given by:

$$\begin{aligned} \rho (v_{,t}(x, t) + (v \cdot \nabla)v(x, t)) &= -\nabla p(x, t) + \mu \nabla^2 v(x, t) \\ &+ f \quad \forall x \in \Omega \\ \nabla \cdot v(x, t) &= 0, \end{aligned} \quad (1)$$

where f denotes all body forces, ρ denotes density, μ denotes the blood viscosity, v denotes velocity, p denotes pressure, and Ω denotes the patient-specific problem geometry. Finite element simulations have emerged as a powerful and robust tool to solve these equations in complex patient-specific geometries [20]–[22]. Fig. 1 shows the important steps in calculating FFR_{CT} from a CT-scan. First, the coronaries of interest are isolated and reconstructed along with a portion of the ascending aorta. An anisotropic finite element mesh with boundary layer elements is constructed using a commercially available package, MeshSim (Simmetrix, Inc., Clifton Park, NY, U.S.A.). Boundary conditions are chosen based on cardiac output, aortic pressure and flow demand of the myo-cardium [2]. These are further modified to mimic hyperemic conditions under administration of adenosine [2]. Finally, the resulting non-linear equations are solved using a stabilized finite element including a Newton-Raphson method based on repeated calls to a linear solver [21].

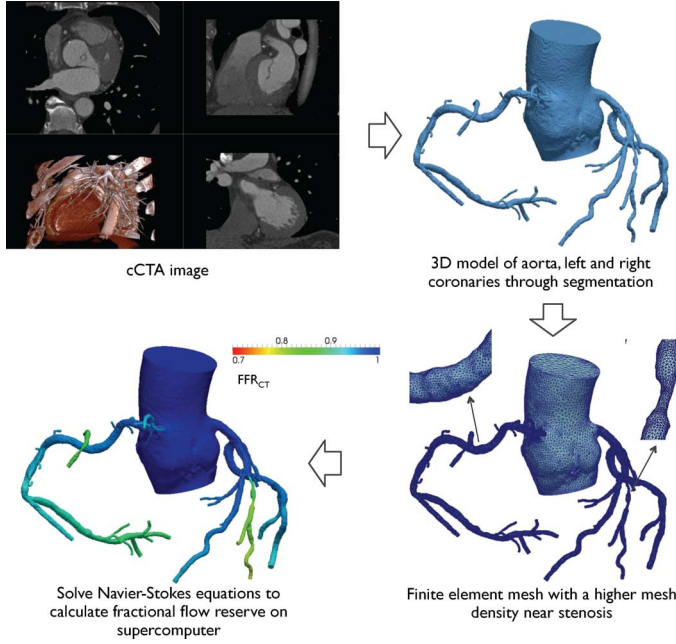


Fig. 1. An overview of the process of calculating FFR_{CT} from cCTA images. The coronary arteries of interest as well as a portion of the aorta are segmented using standard algorithms [23], [25]. The Navier-Stokes equations are solved to calculate FFR_{CT} , which has been shown to have high accuracy in prediction of measured FFR [5].

B. Stochastic Modeling

Calculating sensitivity involves (a) splitting the coronary artery tree into sections and (b) sampling over a set of probable segmentations of the coronary tree. The first step is the extraction of a centerline tree. Centerlines are lines that pass through the interior of the lumen, which are semi-automatically extracted first. Identification of bifurcation and ostium locations is a part of the centerline tree extraction step. An ostium is a location where the coronary arteries intersect the aorta. Various methods for extracting centerlines are described in Schaap *et al.* [23]. These are used as an aid in performing lumen segmentation from which the patient-specific vascular geometry is derived [9]. Centerlines are discretized into distinct points with a spacing of 0.3 mm. The methods described in the rest of the article do not depend on the specific method used for either extraction of the centerline tree or the lumen segmentation.

1) *Parameterizing Geometry*: Uncertainty in lumen segmentation is modeled by first breaking down the coronary tree model into sections, where each section corresponds to lumen segments between two bifurcations, a bifurcation and an outlet, or ostium and a bifurcation. Each section is associated with an independent random variable.

The number of stochastic variables scales with the number of bifurcations and number of outlets, which in turn depends on the size of the coronary tree. A multi-resolution algorithm is described later using which the final sensitivity map does not depend on the bifurcation location.

A random variable is denoted by the symbol ξ . Random variable corresponding to a section j is denoted by ξ^j . Stochastic space of an entire patient specific model is denoted by a vector of random variables

$$\boldsymbol{\xi} = [\xi^1, \xi^2, \dots, \xi^M]$$

Authorized licensed use limited to: Politecnico di Torino. Downloaded on April 15, 2024 at 14:40:11 UTC from IEEE Xplore. Restrictions apply.

where each ξ^j can have any standard or (if available) region specific probability distribution function, and M is the number of sections in the model. A specific realization in the stochastic space is denoted by $\boldsymbol{\xi}_i$ where i denotes a collocation point. The stochastic collocation points corresponding to a section j are represented by ξ_i^j .

The stochastic dimension is discretized using Lagrange polynomials, where velocities and pressures are denoted by $v(x, t, \boldsymbol{\xi}) = \sum_{i=1}^N v(x, t, \boldsymbol{\xi}_i) \mathcal{L}_i(\boldsymbol{\xi})$ and $p(x, t, \boldsymbol{\xi}) = \sum_{i=1}^N p(x, t, \boldsymbol{\xi}_i) \mathcal{L}_i(\boldsymbol{\xi})$ respectively where $\boldsymbol{\xi}_i$ denotes the i^{th} collocation point, x denotes space dimension, N is the number of collocation points, and t denotes the time dimension. The collocation points $\boldsymbol{\xi}_i$ are identified by the adaptive stochastic collocation algorithm [7] where each collocation point corresponds to a distinct geometry.

Although one might be tempted to assign a uniform perturbation for geometric perturbation, such a strategy would not satisfy C^0 continuity. To ensure C^0 continuity, we adopt a Gaussian perturbation model, which is defined as

$$u(\mathbf{c}, \mathbf{c}_o, l, \boldsymbol{\xi}) = u_0(\boldsymbol{\xi}) \frac{1}{\sqrt{2\pi}l} e^{-(d(\mathbf{c}, \mathbf{c}_o)/2l^2)}, \quad (2)$$

where $u_0(\boldsymbol{\xi})$ is the magnitude of uncertainty, \mathbf{c}_o is the center of the section, $d(\cdot, \cdot)$ is the Euclidean distance and the correlation length, l , is set to be 1/6th the length of the section so that the section ends are at a distance $3l$ from center. This ensures negligible perturbation at the section ends, hence ensuring continuity of the finite element mesh at the interface between two neighboring sections. However, when the blood flow simulations are replaced using a machine learning approach, we can use uniform perturbations.

We can also extend the definition above to define perturbations of a point in the arterial wall. These perturbations will be defined as a perturbation ($\Delta \mathbf{a}$) in the co-ordinate of a surface point \mathbf{a} , defined as

$$\Delta \mathbf{a}(\mathbf{c}, \mathbf{c}_o, l, \boldsymbol{\xi}) = u(\mathbf{c}, \mathbf{c}_o, l, \boldsymbol{\xi}) \frac{(\mathbf{a} - \mathbf{c})}{\|\mathbf{a} - \mathbf{c}\|}, \quad (3)$$

where \mathbf{c} is the projection of \mathbf{a} onto the centerline.

C. Governing Equations for Sensitivity Analysis

Since the true patient-specific geometry is unknown (due to resolution, noise in image acquisition, imaging artifacts, etc.), the goal is to solve the Navier-Stokes equations in a family of geometries, Ω^* , such that the true geometry lies within this family. Each geometry in Ω^* is associated with a probability, and we are interested in ensemble properties of blood pressure, and subsequently FFR_{CT} , within Ω^* . Using the stochastic space representation from the previous section, the corresponding stochastic Navier-Stokes equations are given by

$$\begin{aligned} \rho(v_t(x, t, \boldsymbol{\xi}) + (\mathbf{v} \cdot \nabla)v(x, t, \boldsymbol{\xi})) &= -\nabla p(x, t, \boldsymbol{\xi}) \\ &+ \mu \nabla^2 v(x, t, \boldsymbol{\xi}) \\ &+ f \quad \forall x \in \Omega^*(\boldsymbol{\xi}) \\ \nabla \cdot v(x, t, \boldsymbol{\xi}) &= 0. \end{aligned} \quad (4)$$

By using the stochastic collocation method, exact solution of (4) is imposed at the collocation points. Since $FFR_{CT}(x,$

$\xi) = p(x, \xi)/p_{\text{aorta}}$, we can define a FFR_{CT} map for each collocation point i and section j . We denote the FFR_{CT} obtained in the geometry corresponding to i^{th} collocation point at a section j as $\text{FFR}_{\text{CT}}(x, \xi_i^j)$, which is defined as

$$\text{FFR}_{\text{CT}}(x, \xi_i^j) = \frac{p(x, \xi_i^j)}{p_{\text{aorta}}}. \quad (5)$$

Geometric sensitivity is defined as the maximum standard deviation in FFR_{CT} , $\sigma_{\text{FFR}_{\text{CT}}}^*$, due to uncertainty in the segmentation. This value quantifies the maximum impact of changing the cross sectional area of a given section on FFR_{CT} . The stochastic space representation of blood pressure is post-processed to evaluate standard deviation in FFR_{CT} , $\sigma_{\text{FFR}_{\text{CT}}}$ across the coronary model. The geometric sensitivity associated with the section j is, therefore, defined as

$$\sigma_{\text{FFR}_{\text{CT}}}^{*,j} = \max_x \sigma_{\text{FFR}_{\text{CT}}}^j(x) \quad (6)$$

where the standard deviation of FFR_{CT} across the patient-specific geometry, $\sigma_{\text{FFR}_{\text{CT}}}^j(x)$ is calculated as

$$\sigma_{\text{FFR}_{\text{CT}}}^j(x) = \sqrt{\int (\text{FFR}_{\text{CT}}(x, \xi^j) - \overline{\text{FFR}_{\text{CT}}}(x))^2 pdf(\xi^j) d\xi^j}$$

which can be discretized as

$$\sigma_{\text{FFR}_{\text{CT}}}^j(x) = \sqrt{\sum_{i=1}^N (\text{FFR}_{\text{CT}}(x, \xi_i^j) - \overline{\text{FFR}_{\text{CT}}}(x))^2 b_i^j}$$

where $b_i^j = \int \mathcal{L}_i(\xi^j) pdf(\xi^j) d\xi^j$, $\overline{\text{FFR}_{\text{CT}}}(x)$ is the average FFR_{CT} at a given location x , and $pdf(\xi^j)$ is the probability density of ξ^j . The limits of the integration depend on the sample space of pdf (e.g., Gaussian is unbounded, whereas uniform distribution is bounded). Hence, a different probability model can be used, if available, for different sections of the patient-specific model.

Uncertainty analysis on a section of a patient-specific model is illustrated in Fig. 2. The two simulations shown correspond to two collocation points, and sensitivities (not shown) can be obtained by aggregating the FFR_{CT} map obtained for various geometries calculated using the stochastic collocation algorithm, calculating a variance map of FFR_{CT} and calculating the maximum standard deviation for each random variable (or section).

D. Description of Features for Machine Learning

The stochastic collocation method shows significant improvement over Monte-Carlo methods. However, the computational time is still of the order of a few days, and hence not feasible to use in clinical practice. The most time-intensive step in the stochastic collocation method is performing blood flow simulations at the quadrature points. Hence, we use a surrogate model [24] to predict FFR_{CT} . The surrogate model uses a machine learning approach similar to the one used here but is trained on FFR_{CT} instead of sensitivities. All the features used for calculating sensitivities, with the exception of section length and coefficient of variation in lumen area, are used for the surrogate model. A bootstrap aggregated decision tree is used for mapping the features to FFR_{CT} .

Authorized licensed use limited to: Politecnico di Torino. Downloaded on April 15, 2024 at 14:40:11 UTC from IEEE Xplore. Restrictions apply.

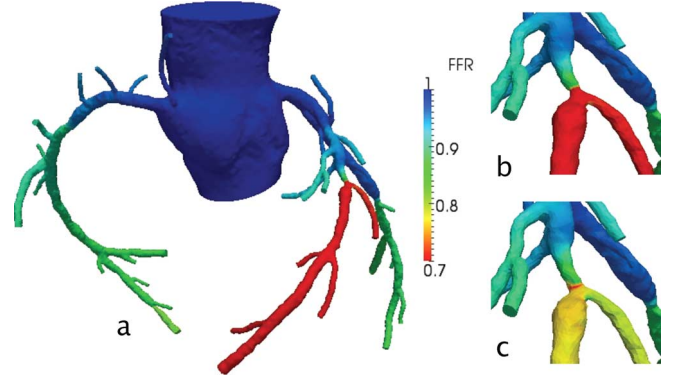


Fig. 2. Impact of error in lumen segmentation in a section on FFR_{CT} is shown for a patient-specific coronary tree geometry. (a) shows FFR_{CT} on the full coronary tree, (b) shows FFR_{CT} in a zoomed-in region near a lesion of interest, and (c) shows the impact of a few voxel variations due to uncertainty in the section containing the lesion. The geometries (b) and (c) correspond to two collocation points, $\xi = 0.5$ and $\xi = 0$ corresponding to the random variable that describes the section containing the lesion. Based on a clinical cutoff of diagnosing disease if $\text{FFR}_{\text{CT}} < 0.8$, there are sections of the coronary tree where diagnosis flips due to a few voxel uncertainty in the lumen segmentation.

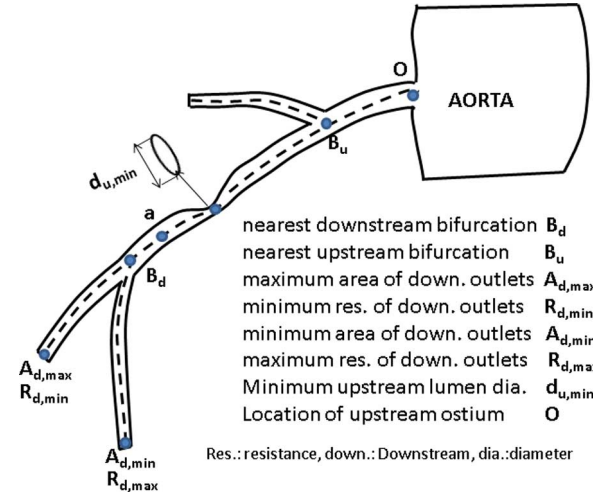


Fig. 3. Schematic of some geometric features used in the machine learning algorithm showing the location of nearest upstream bifurcation, ostium, and minimum upstream diameter, as well as location of nearest downstream bifurcation and outlets with maximum area and resistance, and minimum area and resistance for a given location a .

We first extract salient features from each patient-specific model (refer Fig. 3). Variables which are hypothesized to be relevant to the hemodynamics are included as features for machine learning. These are broadly classified as (a) geometric features, (b) clinical features and (c) reduced order models. We describe each of these below:

1) *Geometric Features*: Reconstructed lumen segmentation is an important variable which determines accuracy of blood flow simulations [15], [6]. We use a data-driven approach, by first discretizing the geometry into points along the centerline of the lumen segmentation, and subsequently representing the lumen segmentation using a vector of geometric descriptors at each centerline point.

Each centerline point in the coronary tree is defined by three classes of properties, namely (a) local, (b) upstream and (c) downstream. Local lumen area is the only local feature

used. Upstream properties include volume of blood upstream, distance to nearest upstream bifurcation, distance to ostium (location where aorta meets coronary artery), minimum upstream diameter, distance along centerline to minimum upstream diameter, number of upstream bifurcations, average upstream diameter, area of nearest upstream bifurcation and area of previous centerline point. Similar properties are also defined for the downstream vascular tree. In addition to these, a lumen narrowing score is introduced, which quantifies how much the lumen is encroached upon based on a theoretical estimate of healthy lumen radius. Note that this measure is similar to the clinically measured % stenosis measure. To define lumen narrowing score, we first introduce a health index score. The health index score is defined as

$$\kappa(x) = \frac{r(x)}{r_h(x)} \quad (7)$$

where $r_h(x)$ is the theoretical healthy radius of the lumen and $r(x)$ is the radius of the maximum inscribed sphere. Shahzad *et al.* [26] described a Gaussian-kernel based estimate to compute healthy lumen radius based on the measured radius. However, the method described there is not directly applicable here due to the significantly larger number of bifurcations, steep variations in healthy lumen radii near bifurcations, and need to capture different forms of lumen reduction such as acute, diffuse, ostial, along bifurcations, etc. Hence, we adapt the method given in Shahzad *et al.* [26] by first defining three different regressors to calculate r_h given by the general form

$$r_h(x) = \frac{\sum_{x'=1}^n \mathcal{N}(x'|x, s_x) S(x', x) w_{x'} r_{x'}}{\sum_{x'=1}^n \mathcal{N}(x'|x, s_x) S(x', x) w_{x'}} \quad (8)$$

where $w_x = \mathcal{N}(r_x | r_{x,\max}, s_{\max})$, n is the number of points used in the regression, $\mathcal{N}(\mu, s)$ is a Gaussian function with mean μ and standard deviation s , and w_x are Gaussian weighting functions. The following regressors are used.

- a global fit, which uses a Gaussian kernel to fit the radius from the ostium to the outlets (the function $S(x', x)$ is unity)
- a sectional fit, which uses a Gaussian kernel but limited within a section bound by the two closest bifurcation locations (the function $S(x', x)$ is unity within the current section and zero in all other sections).
- an anisotropic fit, where the Gaussian kernel is convolved with a sigmoidal kernel centered at the nearest downstream bifurcation location, where the function $S(x', x)$ is defined as

$$S(x', x) = \frac{1}{1 + \alpha e^{-k d_{\text{offset}}(x', x)}},$$

$$d_{\text{offset}}(x', x) = d(x', x_{\text{ostium}}) - d(x, x_{\text{ostium}}) - d(x, x_{\text{up}}),$$

x_{up} is the location of the nearest upstream branch to x and $d(\cdot, \cdot)$ is the Euclidean distance.

Five paired parameter sets were chosen for each of these three regressors, making a total of 15 health index scores. These are given by $s_x = 6 \cdot (1 + (i-3) \cdot 0.4)$, $s_{\max} = 200 \cdot (1 + (i-3) \cdot 0.4)$, $r_{x,\max} = 0.25 \cdot (1 + (i-3) \cdot 0.4)$ and $\alpha = 0.1 \cdot (1 + (i-3) \cdot 0.4)$, where i takes values of 1, 2, 3, 4, 5.

Lumen narrowing scores are calculated as $\delta^i(x) = 1 - \kappa^i(x)$ if $\kappa^i(x) \leq 1$ and zero otherwise, where $\kappa^i(x)$ is the health index score for i^{th} regressor. Fig. 3 shows a schematic of some geometric features used in the machine learning algorithm.

2) *Clinical Features*: In this section, we describe some clinically derived non-geometric features that potentially impacts FFR_{CT}. Since the functional significance of a lesion depends on flow demand of the myocardial bed which in turn depends on myocardial mass, we include myocardial mass as a clinical feature. In addition, aortic blood pressure and body mass index (which depends on height and weight) are added as features. Further, resistance boundary conditions are calculated at each outlet surface which are based on the net coronary flow and resistance of each outlet (which is proportional to the area) [2]. Hence, for each centerline point, six features corresponding to minimum, maximum and mean area and resistances of outlets are calculated and added to the feature set. Blood viscosity, which quantifies resistance of fluid to flow, is also added as a feature. All of these are calculated on a patient-specific basis.

3) *Reduced Order Models*: We assume that the flow split at each branch is inversely related to the net downstream resistance. To calculate the net downstream resistance, we approximate the geometric resistance of a section of the vessel using Poiseuille's law as $R = 8 \mu L / \pi r_{\text{avg}}^4$ and corresponding pressure loss as $\Delta P_i = R Q_i$, where μ is the dynamic viscosity of blood, L is the length of section, r_{avg} is the average lumen radius, Q_i is the flow-rate through the section and ΔP_i is the pressure drop. For tighter stenoses (defined as those with greater than 50%), a non-linear pressure loss proportional to Q_i^2 can be used [27]. It is also possible for the pressure to increase downstream of a narrowing if the downstream area is higher than the upstream area. This is due to the kinetic energy of blood being converted to pressure energy (Bernoulli's equation). Hence we define a pressure recovery feature as $P_{\text{recovery}} = r_{\text{post}} / r_{\text{pre}}$ where r_{post} is the radius distal to the stenosis and r_{pre} is the radius proximal to the stenosis. Distal and proximal are defined based on when the lumen narrowing score becomes zero as we traverse downstream and upstream from the lesion respectively.

E. Adaptive Multi-Resolution Algorithm

The sensitivity analysis above is based on a specific definition of the stochastic space, which depends on the initial lumen segmentation. This stochastic space depends on the location and number of bifurcations and outlets. For instance, the right coronary artery (RCA) has far few bifurcations and hence, has a larger section length compared to the left anterior descending artery (LAD) or the left circumflex artery (LCx). Further, a missed bifurcation could change the sensitivity values assigned to different parts of the coronary geometry. Adaptive multi-resolution analysis achieves two objectives – (i) it removes dependence of the sensitivity map on either the sectional length or bifurcation location, and (ii) it localizes regions of high sensitivity

Algorithm 1 Algorithm framework for performing adaptive multi-resolution sensitivity analysis.

```

Compute sensitivity
for  $\forall s_j \in \mathcal{S}$  do
    sectional_sensitivity( $s_j$ .begin(),  $s_j$ .end())
end for
output sensitivity map
sectional_sensitivity( $a, b$ )
compute_features
compute sensitivities  $\sigma_{FFRCT}^*$ 
set  $l = b - a$ , resolution = 6 mm and  $\sigma_c = 0.05$ .
while  $\sigma_{FFRCT}^* \geq \sigma_c$  &  $l >$  resolution do
    sectional_sensitivity( $a, (a + b)/2$ ).
    sectional_sensitivity( $((a + b)/2, b)$ ).
end while

```

within sections and helps focus user edits to a smaller region in the coronary model.

The first step of multi-resolution analysis is to perform a sectional sensitivity analysis. Sections whose sensitivities are above a chosen cutoff are split further at the mid-point. Hence, every section which has a sensitivity above a cutoff is split into two equal parts. Sensitivity analysis is recursively performed on these two sections until the size of a section falls below a pre-chosen spatial resolution. Hence, we obtain a sensitivity map that spatially resolves regions of high sensitivity. This helps efficient user review of the lumen segmentation by localizing sensitivity within sections to a chosen spatial resolution. Details of implementing the algorithm is given in Algorithm 1.

F. Gather Data From Multiple Patients and Compute Sensitivities

The stochastic collocation algorithm [7] is first used to calculate the sensitivities in all patients. Following this, all the features described in Section II are calculated. Lower order statistics of the features within each section are aggregated (mean, standard deviation, minimum and maximum values). A set of 240 patients from two clinical trials are randomly split into a training set of 158 patients and a test set of 82 patients.

A list of all the features used, along with minimum and maximum values of the features used in the training set are reported in Table I.

G. Use Machine Learning to Estimate Sensitivity

Bootstrap aggregated decision trees [28], having a linear dependence of sensitivity on the features at the leaves, are used to train the sensitivity data. Bootstrapping helps avoid over-fitting the machine learning regressor on the training set. The Weka library [29] is used to find the optimal bootstrap aggregated decision tree. Further, to demonstrate the utility of the three classes of features, namely geometric, clinical and reduced order model, we first compute the optimal regressor using only geometric features and analyze the correlation and mean absolute error between predicted and actual sensitivities. Then, we include the clinical features and compute the performance of the resulting optimal regressor. Finally, all the three classes of features are included and the performance is computed. Since some clinical features depend on geometry (e.g., resistance depends on outlet area), we analyze results only with a combination of clinical and geometric features, and not clinical features in isolation. Similarly, the reduced order features have a dependence on geometric and clinical features.

TABLE I

FEATURES USED IN THE MACHINE LEARNING ALGORITHM, AND THEIR MINIMUM AND MAXIMUM VALUES IN THE TRAINING SET. DISTANCES ARE IN mm, AREAS IN mm^2 AND VOLUME IN mm^3 UNLESS OTHERWISE SPECIFIED. SYSTOLIC AND DIASTOLIC PRESSURES ARE IN MILLIMETERS OF MERCURY, MYOCARDIAL MASS IS IN GRAMS, AND PRESSURE DROP AND RESISTANCES ARE IN $\text{g}/\text{mm}/\text{s}^2$ AND $\text{g}/\text{mm}^4/\text{s}$ RESPECTIVELY

| feature name | minimum | maximum |
|--|---------|---------|
| number of downstream bifurcations | 0 | 57 |
| total downstream volume | 2.51 | 14947.8 |
| average downstream diameter | 0.54 | 2.77 |
| minimum downstream diameter | 0.05 | 0.94 |
| distance to minimum downstream diameter | 0.08 | 185.00 |
| area of nearest downstream bifurcation | 0.25 | 22.07 |
| distance to nearest downstream bifurcation | 4.44 | 187.23 |
| number of downstream outlets | 1 | 58 |
| total area of downstream outlets | 0.49 | 53.79 |
| inlet area | 0.58 | 1109.84 |
| lumen area | 0.36 | 34.26 |
| mean outlet resistance | 3.18 | 227.39 |
| estimated flow | 0.01 | 1.46 |
| estimated pressure | 9511 | 16000 |
| systolic pressure | 100 | 170 |
| diastolic pressure | 55 | 100 |
| height (cm) | 148 | 181 |
| weight(kg) | 47 | 96 |
| myocardial mass | 64 | 282 |
| number of upstream bifurcations | 0 | 18 |
| total upstream volume | 4.61 | 8960.48 |
| average upstream diameter | 1.34 | 29.08 |
| minimum upstream diameter | 0.05 | 0.94 |
| distance to minimum upstream diameter | 0 | 130.99 |
| area of nearest upstream bifurcation | 0.25 | 22.07 |
| distance to nearest upstream bifurcation | 0 | 102.32 |
| distance to ostia | 0.0 | 200.43 |
| is stenotic | 0 | 1 |
| net geometric resistance | 0.01 | 11.42 |
| geometric resistance | 0.01 | 0.763 |
| highest upstream disease burden (15) | 0.12 | 1.00 |
| pressure recovery factor | 1.00 | 2.00 |
| coefficient of variation in lumen area | 0.05 | 0.29 |
| FFR using machine learning | 0.20 | 0.97 |
| section length | 0.11 | 106.15 |

H. Estimation of Allowable Variation in Lumen Area

To understand the relationship between geometric sensitivity and variability in lumen area, the sensitivities are divided into bins of size 0.01 and the coefficient of variation in lumen area within each bin is calculated. For instance, if the maximum allowable sensitivity is 0.05, then all the data points whose sensitivities are between 0.045 and 0.055 are pooled together. The corresponding coefficient of variation are also binned in steps of 0.01 and a histogram is constructed. The number of samples within each bin in the histogram is normalized to yield a probability value. These probabilities are then presented in a surface plot to understand the relationship between a given allowable sensitivity value and the range of c.o.v. in lumen area associated with it.

III. RESULTS

First, we describe the relationship between the lumen narrowing score and both measured FFR and FFR_{CT} . We then demonstrate that geometric data alone is not a sufficient predictor of sensitivity of FFR_{CT} to changes in geometry. We then describe results using the multi-resolution analysis and illustrate its ability to localize segments with high sensitivity. Finally, we calculate the allowable coefficient of variation in lumen areas for a given allowable sensitivity, and observe that it has a strong relation with maximum allowable sensitivity.

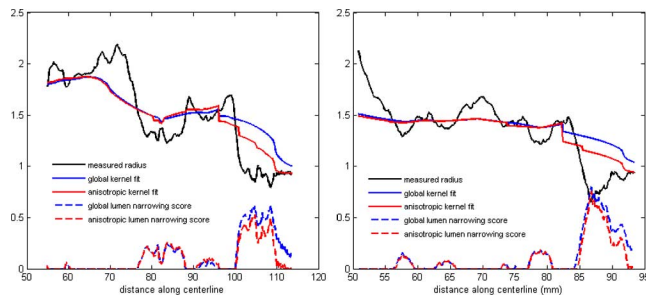


Fig. 4. Comparison of global and anisotropic lumen narrowing scores on two vessels in two different patients illustrating that the methods are similar in most of the coronary tree, but the anisotropic kernel is more accurate in terminal branches, and accounts for natural reduction in radii near bifurcations better.

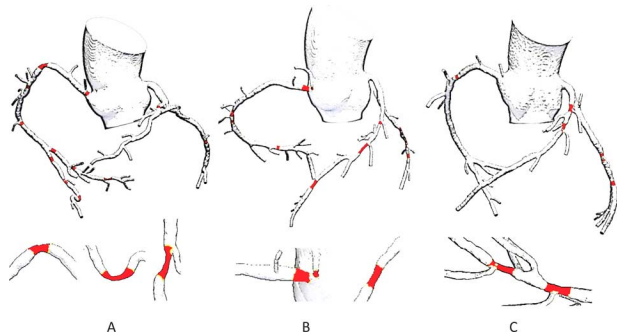


Fig. 5. Maximum lumen narrowing score, calculated as $\Delta_{\max}(x) = \max_i(\delta^i(x))$ over all the 15 regressors, is shown for three patient-specific models with lesions of different size, shapes and locations. Start and end of lesions are modeled based on when $\Delta_{\max}(x)$ crosses a threshold of 0.1. Model A demonstrates that the algorithm is able to capture focal lesions. Model B illustrates an example with a lesion near ostium which is also captured by the lumen narrowing score. Model C illustrates the lumen narrowing score on two lesions across bifurcations. All regions with non-zero Δ_{\max} are colored red.

Fig. 4 highlights the difference in lumen narrowing score between global and anisotropic kernels. An anisotropic kernel allows for the natural variation in radii at bifurcations, as hypothesized by Murray's law (the cube of parent vessel radius is sum of cube of daughter vessel radii). By construct, the global and anisotropic kernel regression are identical in regions away from bifurcations. However, the global kernel may not be accurate at bifurcations with steep reduction in area, which is observed in terminal vessels.

Additionally, the 15 different lumen narrowing scores are aggregated by calculating the highest lumen narrowing score. Fig. 5 shows the aggregate measure on three different patient-specific models, capturing focal lesions, lesions near ostium, and bifurcations. While a direct validation of this score is only possible by comparison to invasively measured % stenosis score, we compare the highest upstream lumen narrowing score against both measured FFR and FFR_{CT} . Fig. 6 shows a scatter-plot of the highest upstream lumen narrowing score to both measured and simulated FFR, with correlation coefficients of 0.42 and 0.48 respectively.

A comparison of the performance of the machine learning algorithm on the testing set indicated that a bootstrap aggregated decision tree regressor was optimal. Other candidate regressors that were attempted were linear regressor, bagged decision tree with linearly interpolated value at the leaves, and

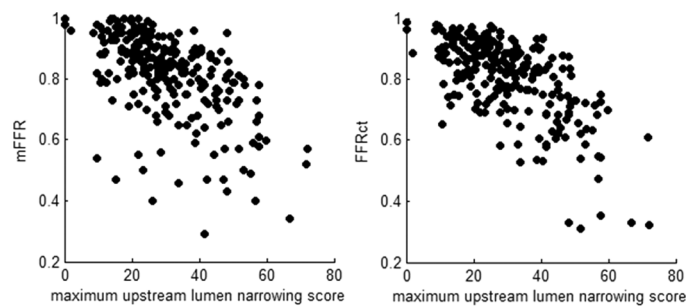


Fig. 6. Comparison of the highest upstream lumen narrowing score and (left) measured FFR and (right) FFR_{CT} with correlation coefficients of 0.42 and 0.48 respectively.

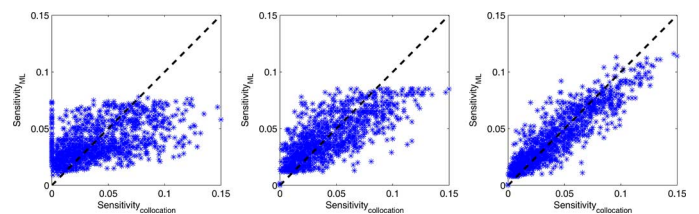


Fig. 7. Comparison of the optimal machine learning regressor on the test set using (left) only geometric features, (center) geometric and clinical features and (right) geometric, clinical and reduced order model features. The figure demonstrates that we get an increased degree of correlation as we include the different class of features defined in Section II. Each point represents a section of a vessel, and there are around 50 sections per subject dataset. The graph was constructed over a test dataset of 82 subjects. The correlation coefficients for the three plots are (from left to right) 0.53, 0.80 and 0.91 respectively. The corresponding mean absolute error are 0.0195, 0.0137 and 0.0094 respectively.

decision stump. We achieved a correlation coefficient of 0.91, mean absolute error of 0.0094 and root mean square error of 0.013 using the bagged decision tree regressor. Fig. 7 compares the relationship between sensitivities calculated using only the geometric features, geometric and clinical features, and all the features that are detailed in Section II. This clearly demonstrates that each of the classes of features adds value to the performance of the final machine learning regressor, with correlation coefficients of 0.53, 0.80 and 0.91 respectively.

Multi-resolution sensitivity maps for a patient-specific geometry based on an uniform probability distribution function are shown in Fig. 8. The figure shows sensitivity maps computed using sectional sensitivity analysis and using multiresolution analysis with parameters of 15 mm, 9 mm and 6 mm. Using sectional sensitivity analysis, entire sections of high sensitivity are highlighted. Hence, sectional sensitivity analysis may not offer significant savings in user review time if there are sections of large length without branching vessels. In contrast, multi-resolution analysis helps refine sensitivities in sections of large length. For instance, multi-resolution analysis can help reduce review time in a section of length 100 mm by around a factor of 15 if we set the multi-resolution threshold as 6 mm. Four different highlighted lesions in the figure show that multi-resolution analysis offers a significant reduction in the size of the region considered for user review. The highlighted regions represent localized regions in the lumen segmentation which has maximum impact on FFR_{CT} , and hence diagnostic performance.

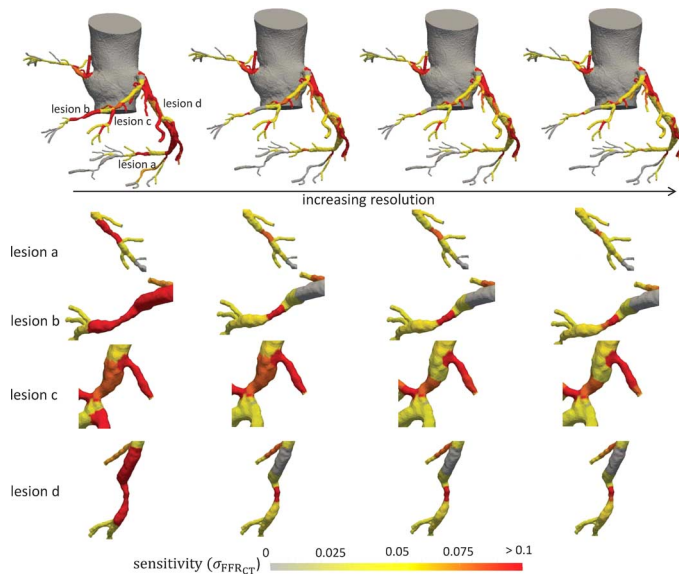


Fig. 8. Illustration of sensitivity map in the coronary arteries in a patient using (from left to right) sectional sensitivity analysis, and multi-resolution analysis with minimum length scale of 15 mm, 9 mm and 6 mm. The corresponding sensitivities for four isolated lesions are also highlighted, demonstrating that multi-resolution sensitivity analysis could localize regions of high sensitivity within a section at a reduced computational overhead.

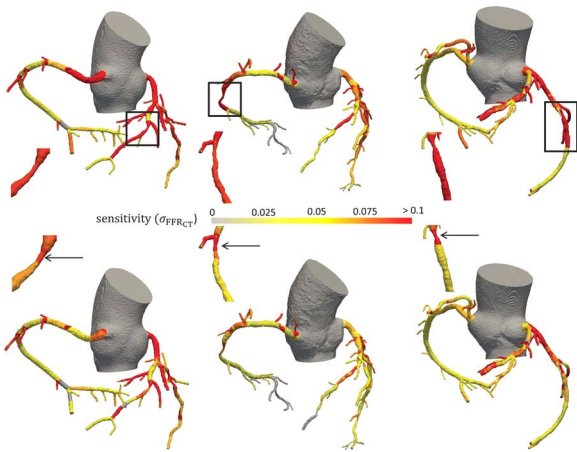


Fig. 9. Comparison of sectional sensitivity analysis (top) and multi-resolution sensitivity analysis (bottom) for three patient-specific coronary arteries. Sections of high sensitivity are highlighted for each patient, and the effect of adaptive multi-resolution analysis in localizing region of high sensitivity to a lesion is depicted. Adaptive multi-resolution sensitivity analysis helps reduce review time from inspecting entire sections of high sensitivity to the relevant localized regions within each section.

A comparison of sectional and adaptive multi-resolution sensitivity analysis on three patients is shown in Fig. 9. Isolated lesion sections are enlarged to illustrate how multi-resolution analysis is able to focus the user on the most sensitive locations within a section. Multi-resolution analysis enables a more focused user review in regions within sections of high sensitivity.

Finally, we compute the range of allowable standard deviation in lumen area for a given maximum allowable sensitivity. A surface plot with the probabilities calculated for each sensitivity bin is shown in Fig. 10. We observed a monotonic increase in the peak allowable coefficient of variation in lumen area, with

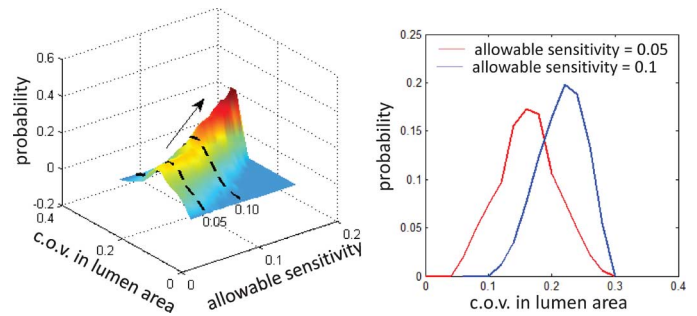


Fig. 10. Surface plot of probability distributions of allowable coefficient of variation (ratio of standard deviation to mean value) in lumen area for a range of allowable sensitivity values is shown on the left, demonstrating that if the allowable sensitivity is higher, then the normalized standard deviation in lumen area can be higher. Comparison of the probability distribution of allowable coefficient of variation in lumen area for a given desired error in FFR_{CT}. Average allowable coefficient of variation for an allowable error of 0.05 is 16% and average allowable coefficient of variation for an allowable error of 0.1 is 21%. The 5th percentile values corresponding to errors of 0.05 and 0.1 are 6% and 11% respectively.

the 5th percentile values for allowable sensitivities of 0.05 and 0.1 being 6% and 11% respectively. The observed differences also illustrates the relationship between segmentation accuracy and simulation accuracy.

IV. DISCUSSION

Sensitivity analysis quantifies how local lumen segmentation affects global hemodynamics. Here, we focused on a hemodynamically derived quantity of interest used in diagnosis of coronary disease, namely FFR_{CT}. Sections of lumen are chosen and they are assigned a sensitivity value based on the worst impact of uncertainty in the sectional lumen area on FFR_{CT}. In general, the magnitude of uncertainty in lumen segmentation might depend on image quality, e.g., contrast-to-noise ratio, presence of artifacts such as mis-registration or motion, etc [30]. Using the framework developed here, different sections can have not just different coefficient of variations, but also different probability distribution function using a different random variable ξ^j associated with each section. For example, lumen segmentation in the vicinity of misalignment or blooming artifact can be modeled to have a different coefficient of variation compared to the rest of the coronary tree.

We quantified sensitivities in near real time using a machine learning approach. A combination of geometric, clinical and reduced-order features were used as features and a database of patient-specific geometries and parameters were used to train the data. A hybrid approach for quantifying lumen narrowing score was used, and is able to detect regions of lumen narrowing for focal lesions, those near bifurcations and ostia. A direct validation of the lumen narrowing score is only possible by comparing these values against those measured by a trained cardiologist. The correlation coefficient between lumen narrowing score and the measured FFR was 0.42, which was comparable to values that were clinically reported (correlation of 0.32) [31]. The correlation coefficient between lumen narrowing score and FFR_{CT} was 0.48. We achieve a good performance using the machine learning algorithm, with a correlation coefficient of 0.91 and

mean absolute error of < 0.01 , compared to sensitivities calculated using the stochastic collocation method. Real-time sensitivity analysis enables user review of segmentation only in regions of the coronary tree which affect the hemodynamics, which is a small fraction of the entire coronary tree.

We introduced a method for multi-resolution sensitivity analysis to further focus attention within sections of high sensitivity. The algorithm initializes sensitivity values using sectional sensitivity analysis, and in regions of sensitivity above a cutoff, splits the section into two and re-evaluates sensitivities. The algorithm terminates when either there are no sections with sensitivity larger than cutoff, or when we reach a minimum spatial resolution. Since sensitivities are meaningful only when a section of the vessel is considered, we do not resolve beyond 6 mm. We were able to resolve and localize regions of high sensitivity, and the resultant sensitivity map helps focus attention on a much smaller region compared to sectional sensitivity analysis. Based on results in a few patients, we hypothesize that savings of more than a factor of 10 can be achieved using the multi-resolution algorithm.

It is important to note that regions of high sensitivity are not necessarily regions of lumen narrowing, or vice versa. Segmentation accuracy might be important in vessels that are important for blood transport downstream, e.g., ostial sections, and sections that branch off of left main into LAD and LCx. Similarly, in vessels with serial lesions, it is not possible to analytically predict which lesions will be important. For instance, if a proximal lesion is tighter than the distal lesion, it is likely that proximal lesion would be more sensitive. However, if distal lesion is tighter, then it is not possible to predict analytically which lesion is more sensitive since it is a combination of flow through the lesion and pressure drop across the lesion. Similarly, if a vessel splits and there are lesions on both branches, it is not possible to predict analytically the sensitivities in each of these lesions. The importance of each class of features was demonstrated by comparing the optimal machine learning regressor using only geometric features, and hierarchically including clinical features and reduced order model features. The results showed that the mean absolute error is reduced by around a factor of two between only geometric features and the whole set of features. Similarly, there was a corresponding increase in correlation coefficient from 0.52 to 0.91.

Fig. 11 illustrates three vessels where high sensitivities are not necessarily regions of highest lumen narrowing score. In all cases, the proximal section closest to the ostium has moderate to high sensitivity since they are important to blood transport and under-segmentation would drop blood flow through the rest of the vessel. In the first case, a mid-lesion of large stenosis severity is most sensitive while the rest are not, whereas in the last example, both proximal and mid-lesions are sensitive. If there is a lesion on each of two vessels that bifurcate of a parent vessel, the relative ratio of lesion resistance to downstream boundary resistance of the vessels will be an important factor in the determination of sensitivity information.

We also compared the allowable coefficient of variation in lumen area for a given allowable standard deviation in FFR_{CT} . The results showed that less than a 6% coefficient of variation in lumen area will translate into a sensitivity of FFR_{CT} of less than

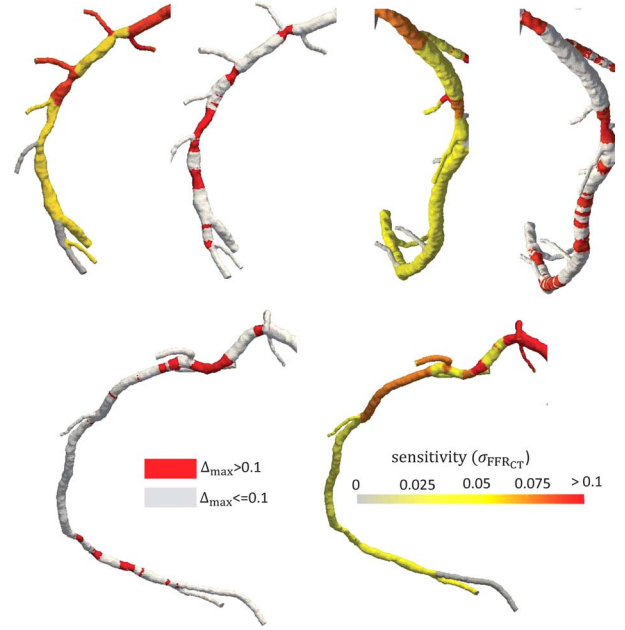


Fig. 11. Map of lumen narrowing score in three vessels juxtaposed with the corresponding multi-resolution sensitivity maps, illustrating that regions of high sensitivity are not necessarily regions of largest lumen narrowing. All the three vessels indicate that sensitivity in proximal vessels could be high even in the absence of disease, since they are critical to blood transport and under-segmentation impacts diagnosis. Figure on top left illustrates an example of four serial lesions and the second lesion dominating, which can only be computed using accurate flow modeling. The figure on the top right illustrates an example where a proximal lesion is the highly sensitive lesion, whereas the figure on the bottom illustrates an example of two sensitive lesions in a vessel.

0.05 with 95% confidence. Similarly, a coefficient of variation in lumen area of less than 11% will translate into a sensitivity of less than 0.10 with 95% confidence. In other words, based on the accuracy of lumen segmentation algorithm, an assessment of error in FFR_{CT} can be made.

One limitation of our algorithm is that the results depend on the initial segmentation. The impact of this dependence was reduced by using the multi-resolution algorithm, but a dependence still exists. For instance, if a lumen narrowing is entirely missed in the initial segmentation, sensitivity information will not be captured unless the uncertainty zone encompasses the true lumen. Hence, a more accurate uncertainty model that accounts for image quality and initial lumen segmentation is needed to enable sensitivity computation when initial segmentation is poor. Another limitation of this work is that the uncertainty in flow and pressure at bifurcations is not calculated using CFD for the ground truth, hence they are not captured using the perturbation model used in this work. Also, it is not well understood if the uncertainty in different lesions are correlated. While our manual correction process (user edits) are not correlated across lesions, modeling correlation might help better assess overall uncertainty of FFR_{CT} at measurement locations. Further, the geometric sensitivity near regions of bifurcations are not captured in the training dataset.

In conclusion, we developed a method that calculates and outputs regions of a coronary vessel tree based on impact of a local vessel section on global hemodynamics. We demonstrate that

regions of anatomic narrowing are correlated poorly with regions of high sensitivity, and the true impact of segmentation can only be assessed using a combination of flow modeling, pressure drop and downstream resistance. We also developed a multi-resolution algorithm that spatially refines regions of high sensitivities to a desired resolution. This significantly reduces the overhead for user edits of lumen segmentation compared to editing the entire lumen segmentation. However, correlations between different parts of the lumen are not modeled. Also, we assumed that the true geometry is encompassed within the limits of the stochastic space that is explored, which may not be accurate in some extremal cases.

REFERENCES

- [1] P. A. L. Tonino *et al.*, "Fractional flow reserve versus angiography for guiding percutaneous coronary intervention," *N. Eng. J. Med.*, vol. 360, no. 3, pp. 213–224, 2009.
- [2] C. A. Taylor, T. A. Fonte, and J. K. Min, "Computational fluid dynamics applied to cardiac computed tomography for noninvasive quantification of fractional flow reserve: Scientific basis," *JACC*, vol. 61, no. 22, pp. 2233–2241, 2013.
- [3] B. K. Koo *et al.*, "Diagnosis of ischemia-causing coronary stenoses by noninvasive fractional flow reserve computed from coronary computed tomographic angiograms results from the prospective multicenter DISCOVER-FLOW study," *JACC*, vol. 58, no. 19, pp. 1989–1997, 2011.
- [4] J. K. Min *et al.*, "Diagnostic accuracy of fractional flow reserve from anatomic CT angiography," *J. Am. Med. Assoc.*, vol. 308, no. 12, pp. 1237–1245, 2012.
- [5] B. L. Norgaard *et al.*, "Diagnostic performance of non-invasive fractional flow reserve derived from coronary CT angiography in suspected coronary artery disease: The NXT trial," *J. Am. Coll. Cardiol.*, 2014.
- [6] J. A. Moore, D. A. Steinman, and C. R. Ethier, "Computational blood flow modelling: Errors associated with reconstructing finite element models from magnetic resonance images," *J. Biomechan.*, vol. 31, no. 2, pp. 179–184, 1998.
- [7] S. Sankaran and A. L. Marsden, "A stochastic collocation method for uncertainty quantification and propagation in cardiovascular simulations," *J. Biomechan. Eng.*, vol. 133, pp. 031001–1, 2011.
- [8] C. A. Figueroa *et al.*, "Predicting patient-specific hemodynamics at rest and stress through an aortic coarctation," presented at the MICCAI, Nagoya, Japan, 2013.
- [9] M. Schaap *et al.*, "Robust shape regression for supervised vessel segmentation and its application to coronary segmentation in CTA," *IEEE Trans. Med. Imag.*, vol. 30, no. 11, pp. 1974–1986, Nov. 2011.
- [10] S. Voros *et al.*, "Prospective validation of standardized, 3D, quantitative coronary computed tomographic plaque measurements using radiofrequency backscatter IVUS as reference standard in intermediate coronary arterial lesions," in *JACC Cardiovasc. Intervent.*, Apr. 2, 2011, pp. 198–208.
- [11] N. Agarwal and N. R. Aluru, "A domain adaptive stochastic collocation approach for analysis of MEMS under uncertainties," *J. Comput. Phys.*, vol. 228, no. 20, pp. 7662–7688, 2009.
- [12] G. Lin, A. M. Tartakovsky, and D. M. Tartakovsky, "Uncertainty quantification via random domain decomposition and probabilistic collocation on sparse grids," *J. Comput. Phys.*, vol. 229, no. 19, pp. 6995–7012, 2010.
- [13] H. N. Najm, "Uncertainty quantification and polynomial chaos techniques in computational fluid dynamics," *Annu. Rev. Fluid Mechan.*, vol. 41, pp. 35–52, 2009.
- [14] Y. Hoi *et al.*, "Validation of CFD simulations of cerebral aneurysms with implication of geometric variations," *J. Biomechan. Eng.*, vol. 128, no. 6, pp. 844–851, 2006.
- [15] J. R. Cebral *et al.*, "Efficient pipeline for image-based patient-specific analysis of cerebral aneurysm hemodynamics: Technique and sensitivity," *IEEE Trans. Med. Imag.*, vol. 24, no. 4, pp. 457–467, Apr. 2005.
- [16] S. Sankaran and A. L. Marsden, "The impact of uncertainty on shape optimization of idealized bypass graft models in unsteady flow," *Phys. Fluids*, vol. 22, no. 12, p. 121902, 2010.
- [17] D. Xiu and J. S. Hesthaven, "High order collocation methods for the differential equation with random inputs," *J. Sci. Comput.*, vol. 27, pp. 1118–1139, 2005.
- [18] D. Xiu and G. E. Karniadakis, "Modeling uncertainty in steady state diffusion problems via generalized polynomial chaos," *Comput. Methods Appl. Mechan. Eng.*, vol. 191, pp. 4927–4948, 2002.
- [19] M. Sermesant, H. Delingette, and N. Ayache, "An electromechanical model of the heart for image analysis and simulation," *IEEE Trans. Med. Imag.*, vol. 25, no. 5, pp. 612–625, May 2006.
- [20] C. A. Taylor, T. J. R. Hughes, and C. K. Zarins, "Finite element modeling of blood flow in arteries," *Comput. Methods Appl. Mechan. Eng.*, vol. 158, no. 1–2, pp. 155–196, 1997.
- [21] H. J. Kim *et al.*, "Patient-specific modeling of blood flow and pressure in human coronary arteries," *Ann. Biomed. Eng.*, vol. 38, no. 1, pp. 3195–3209, 2010.
- [22] C. A. Taylor, T. J. R. Hughes, and C. K. Zarins, "Computational investigations in vascular disease," *Comput. Phys.*, vol. 10, no. 3, pp. 224–232, 1996.
- [23] M. Schaap *et al.*, "Standardized evaluation methodology and reference database for evaluating coronary artery centerline extraction algorithms," *Med. Image Anal.*, vol. 13, no. 5, pp. 701–714, 2009.
- [24] S. Sankaran, L. Grady, and C. A. Taylor, "Real-time sensitivity analysis of blood flow simulations to lumen segmentation uncertainty," in *Medical Image Computing and Computer-Assisted Intervention—MICCAI 2014*, 2014, Lecture Notes Comput. Sci., pp. 1–8.
- [25] D. Lesage *et al.*, "A review of 3D vessel lumen segmentation techniques: Models, features and extraction schemes," *Med. Image Anal.*, vol. 13, no. 6, pp. 819–845, 2009.
- [26] R. Shahzad *et al.*, "Detection and quantification of coronary artery stenoses on CTA," *Int. J. Cardiovasc. Imag.*, vol. 29, pp. 1–13, 2013.
- [27] Y. Huo, M. Svensden, J. S. Choy, Z. D. Zhang, and G. S. Kassab, "A validated predictive model of fractional flow reserve," *J. R. Soc. Interface*, vol. 9/71, pp. 1325–1338, 2011.
- [28] L. Breiman, "Bagging predictors," *Mach. Learn.*, vol. 24, no. 2, pp. 123–140, 1996.
- [29] M. Hall *et al.*, "The WEKA data mining software: An update," *SIGKDD Explorat.*, vol. 11, no. 1, 2009.
- [30] J. F. Barrett and N. Keat, "Artifacts in CT: Recognition and avoidance 1," *Radiographics*, vol. 24/6, pp. 1679–1691, 2004.
- [31] W. Meijboom *et al.*, "Comprehensive assessment of coronary artery stenoses: Computed tomography coronary angiography versus conventional coronary angiography and correlation with fractional flow reserve in patients with stable angina," *J. Am. Coll. Cardiol.*, vol. 52, no. 8, pp. 636–643, 2008.